Available online at www.sciencedirect.com
SCIENCE DIRECT
Journal of Power Sources 153 (2006) 114–124
JOURNAL OF POWER SOURCES
www.elsevier.com/locate/jpowsour

Electrical and microstructural characterization of spinel phases as potential coatings for SOFC metallic interconnects

William Qu [a], Li Jian [b], Josephine M. Hill [a], Douglas G. Ivey [c,*]

[a] *Department of Chemical and Petroleum Engineering, University of Calgary, Calgary, Alta., Canada T2N 1N4*
[b] *School of Materials Science and Engineering, State Key Laboratory of Plastic Forming Simulation and Die and Mould Technology, Huazhong University of Science and Technology, Wuhan, Hubei 430074, PR China*
[c] *Department of Chemical and Materials Engineering, University of Alberta, Edmonton, Alta., Canada T6G 2G6*

Received 17 February 2005; accepted 22 March 2005
Available online 13 June 2005

Abstract

Several spinel samples, i.e., $Mn_xCr_{3-x}O_4$ ($0.5 \leq x \leq 2.5$), $NiCr_2O_4$ and $CoCr_2O_4$, were synthesized and studied in terms of phase analysis, density, electrical resistivity and thermal expansion behaviour. The spinel samples were generally single phase; exceptions included $MnCr_2O_4$ and $Mn_{0.5}Cr_{2.5}O_4$ with significant amounts of Cr_2O_3 and $NiCr_2O_4$ with trace amounts of NiO.

Porosity, in general, decreased with increasing sintering temperature, except for $Mn_{0.5}Cr_{2.5}O_4$, which showed increasing porosity with increasing sintering temperature. $NiCr_2O_4$, $CoCr_2O_4$ and $MnCr_2O_4$, all had similar thermal expansion behaviour, with thermal expansion coefficients (TEC) ranging from $7.2–7.6 \times 10^{-6}/°C$. The TEC difference between the spinels and ferritic stainless steel was larger than the difference between the steel and chromia, which had a TEC of $9.6 \times 10^{-6}/°C$. The spinels and chromia exhibited semiconductor-type behaviour, with electrical resistivities decreasing with increasing temperature. Only Mn_2CrO_4 and $NiCr_2O_4$ had resistivities lower than Cr_2O_3 over the entire temperature range of testing (20–900 °C). For $Mn_xCr_{3-x}O_4$, resistivity decreased with increasing Mn content.

Keywords: Spinels; Resistivity; Microstructure; Interconnect; Solid oxide fuel cell

1. Introduction

The interconnect is a critical component in solid oxide fuel cells (SOFCs). Interconnects provide physical separation between air and fuel in the SOFC stack and electronically connect an anode of one cell with the cathode of the adjacent cell. Interconnects must be good electronic conductors and must retain good interconnect-electrode contact in both oxidizing and reducing atmospheres. In recent years, increasing attention has focused on finding suitable metallic materials for interconnects because of their low fabrication costs and good electronic and thermal conductivities, relative to ceramic alternatives. Among the various metallic candidates, ferritic stainless steels may be an economical choice for planar, anode supported designs, which operate at temperatures below 800 °C. A major drawback in using ferritic alloys (or any alloys) in SOFCs is high temperature oxidation. Oxidation not only leads to dimensional changes and loss in load bearing cross sections of the components, but also in the formation of oxide scales on component surfaces which generally have low electronic conductivities [1].

Recent studies have shown that the main oxides forming on ferritic stainless steels are chromia (Cr_2O_3) and $MnCr_2O_4$ spinel [2–4]. Other spinels, containing Cr, Mn, Fe, Co and Ni, can form; the compositions depend on the composition of the steels and any other materials in contact with the interconnects. Some researchers have tried to apply spinel layers to the surface of stainless steels in order to improve interconnect oxide electronic conductivity [5,6].

* Corresponding author. Tel.: +1 780 492 2957; fax: +1 780 492 2881.
E-mail address: doug.ivey@ualberta.ca (D.G. Ivey).

0378-7753/$ – see front matter © 2005 Elsevier B.V. All rights reserved.
doi:10.1016/j.jpowsour.2005.03.137

As an example, a group at the University of Utah have patented Mn–Cr spinel coatings with electronic resistivities significantly lower than chromia [5,6]. Other researchers claim that spinels are responsible for the poor conductivity of high temperature interconnect materials [4,7,8]. Because of the widely varying claims concerning spinels, a systematic study of the properties of spinel phases, in particular those of interest for SOFC interconnects, i.e., those containing elements such as chromium, manganese, nickel and cobalt, is needed to understand the role of spinels in the oxidation of interconnects.

The spinels are a group of oxides that have very similar structures. The spinel group contains over 20 members, but only a few are considered common. The general formula of the spinel group is AB_2O_4. The A element represents a divalent metal ion such as magnesium, iron, nickel, manganese and/or zinc. Tetravalent ions, such as Pb, may also occupy this site. The B element represents trivalent metal ions such as aluminum, iron, chromium and manganese. Many of the transition metals (e.g., Fe, Cr and Mn) are multivalent and, as such, could be both A and B elements. Solid solution substitution is common for this group of minerals, meaning that they may contain certain percentages of different ions in any particular specimen. The structure of spinel is based on the structure of diamond, which has the same high symmetry. The position of the A ions is equivalent to the positions occupied by carbon atoms in the diamond structure [9]. The purpose of this paper is to characterize select spinels with a long term potential aim of choosing prospective candidates for coatings on interconnect alloys. The spinels chosen for study include $MnCr_2O_4$, $NiCr_2O_4$ and $CoCr_2O_4$. $MnCr_2O_4$ spinel was chosen because Mn is a common alloying element in stainless steels and $MnCr_2O_4$ is one of the two main oxides that form on ferritic stainless steels. Since the composition of the Mn spinel phases can vary, other compositions, i.e., $Mn_{0.5}Cr_{2.5}O_4$, $Mn_{1.5}Cr_{1.5}O_4$ and Mn_2CrO_4, are characterized as well. Nickel is a common alloying element in many iron-based alloys (e.g., austenitic stainless). Both Ni and Co can be present in contact pastes, used to bond the fuel cell to the interconnect, and can react with chromia to form spinel phases. In addition to the three spinel phases, the properties of chromia are also studied as it is the other major oxide forming on ferritic stainless steels. The characterization work focuses on resistivity and thermal expansion properties of these spinels, which are the most important properties for SOFC applications.

The spinels were prepared using oxides of manganese, nickel, cobalt and chromium. Ball milling was used to mix stoichiometric compositions of the powder. Mixed powders were then die-pressed into pellets and sintered at 1200 and 1600 °C for 10 h in air. The sintered samples were examined using X-ray diffraction (XRD), scanning electron microscopy (SEM) and energy dispersive X-ray (EDX) spectroscopy. Thermal expansion coefficients (TEC) and electronic resistivities were measured as a function of temperature.

Table 1
Raw material specifications

Chemical	Purity (%)
Cr_2O_3	99
MnO_2	99.9
NiO	99
Co_3O_4	99.7

All chemicals were obtained from Alfa Aesar.

2. Experimental procedure

2.1. Sample preparation

Spinels were synthesized by solid-state reaction of binary oxides (Table 1). All oxide powders were sieved to pass through 325 mesh, which corresponds to a particle size less than 45 μm. The metal oxides were carefully weighed to produce the appropriate stoichiometric mixtures for the spinels of interest. Weighed powders were pre-mixed by ball milling in a plastic bottle overnight, with zirconia as the milling medium and ethanol as a solvent. The resultant slurry was dried in an oven at 70–80 °C for 10 h.

Dried pre-mixed powders were pressed, in the appropriate die, into bars and pellets, using an ENERPAC RC104 press. For each sample, approximately 2 g of mixed powder were weighed and poured into the mould. Top loading was applied to a pressure of 10,000 kPa for 1 min. No binder was added to the powder; naturally absorbed moisture served as a binder. Care was taken to ensure that pressures did not exceed 10,000 kPa; otherwise, internal cracks would be generated in the pellets and bars. The cracks were not always apparent on visual inspection, but would develop during sintering and result in pellet/bar failure. If the pressure was less than 7500 kPa, the green pellet or bar was not strong enough for handling. Green bars and pellets were sintered in air at 1200 and 1600 °C, respectively, for 10 h with a heating rate of 3 °C/min. Sintered specimens were furnace cooled to room temperature in about 10 h. A temperature of 1600 °C was chosen, based on the Mn_2O_3–Cr_2O_3 phase diagram [10], so that diffusion and therefore reaction rates could be maximized without the formation of any liquid. Samples were also sintered at 1200 °C so that results could be compared with those from other groups.

2.2. Spinel characterization

2.2.1. TEC measurements

Thermal expansion coefficients (TEC) for spinels were obtained using a SETARAM Scientific Industrial Setsys16/18 multi function thermal analysis device, integrated with a thermomechanical analysis (TMA) head. The deflection of a given spinel sample under a non-oscillatory load was measured as a function of temperature [11]. TEC samples were rectangular bars with parallel ends, ground mechanically with 600 grit SiC paper to dimensions of 5 mm × 5 mm × 15 mm to fit the measurement jig.

Measurements were performed at a heating rate of 5 °C/min from room temperature (20 °C) to 900 °C. A 25 g top load was applied to each specimen. In order to eliminate the expansion of the alumina probe from the test results, a blank test was run prior to sample testing. Net expansion data were obtained by subtracting measured data from the blank data.

2.2.2. XRD analysis

X-ray diffraction analysis was used for phase analysis of the synthesized spinels, using a Rigaku Multiflex X-ray Diffractometer. Samples were scanned over the range of $2\theta = 15$–90°, in steps of 0.020° and a scan speed of 0.5°/min. The XRD was operated at 40 kV and 40 mA, using a Cu target.

Prior to XRD analysis, sintered pellets were surface ground with 600 grit SiC paper in order to remove surface contamination and to ensure surface flatness. Pellets were held in a 5 mm deep sample jig with an adhesive pad.

2.2.3. SEM analysis

All spinel samples were examined by scanning electron microscopy in a LEO 1450 Variable Pressure SEM, equipped with an Oxford Instruments ultra thin window (UTW) X-ray detector. Both secondary electrons (SE) and backscattered electrons (BSE) were used for imaging to provide topographic (SE) and atomic number (BSE) contrast. Quantitative microanalysis was obtained through energy dispersive X-ray spectroscopy, using a standardless approach.

2.2.4. Resistivity measurements

The electrical resistivities were measured using a 4-point probe system set up inside a tube furnace with a programmable temperature controller (Thermolyne 21100 tube furnace), a constant current supply (Agilent E3610), a custom designed hollow ceramic tube with the end partially cut and a data recorder (Fluke Hydra Series II) (Fig. 1). Platinum mesh and platinum wire were used for contact media and current leads. The platinum mesh was supported by a ceramic tile. Ceramic rods, under compression, were used to apply pressure to the "sandwich" structure during measurement. Springs and rigid metal wires were used to clamp the assembly together. Each platinum mesh had two welded platinum leads. One pair of leads was used to apply a constant current and the other pair was for voltage measurement. A thermocouple was positioned, so it was just touching the bottom ceramic piece, to facilitate temperature measurement.

The specimens were the same as those used for XRD analysis. A spinel pellet was inserted between the platinum meshes. Platinum paste was applied, with a knife blade, to the platinum mesh prior to pellet insertion. A pre-sintering procedure (900 °C for 15 min) was performed before testing. Wet paste was applied again to the specimen pellet before insertion in order to ensure contact. The assembled jig was inserted into a tube furnace. The heating rate for the measurement was 1 °C/min to 900 °C followed by furnace cooling to room temperature. A 0.1 A constant current was applied during measurement. Voltage changes were recorded at a rate of one reading per minute.

2.3. Porosity measurements

The porosity of the sintered samples was measured according to Archimedes principle. De-ionized water was used as the fluid, and the porosity P was calculated from the following equation, assuming negligible enclosed porosity:

$$P = \frac{V_1}{V_2} = \frac{(W_3 - W_1)}{W_2} \quad (1)$$

V_1 and V_2 are the total pore volume within a specimen and the volume of the specimen, respectively, W_1 is the mass of a dry specimen, W_2 is the buoyancy force in water and W_3 represents the mass of a wet sample.

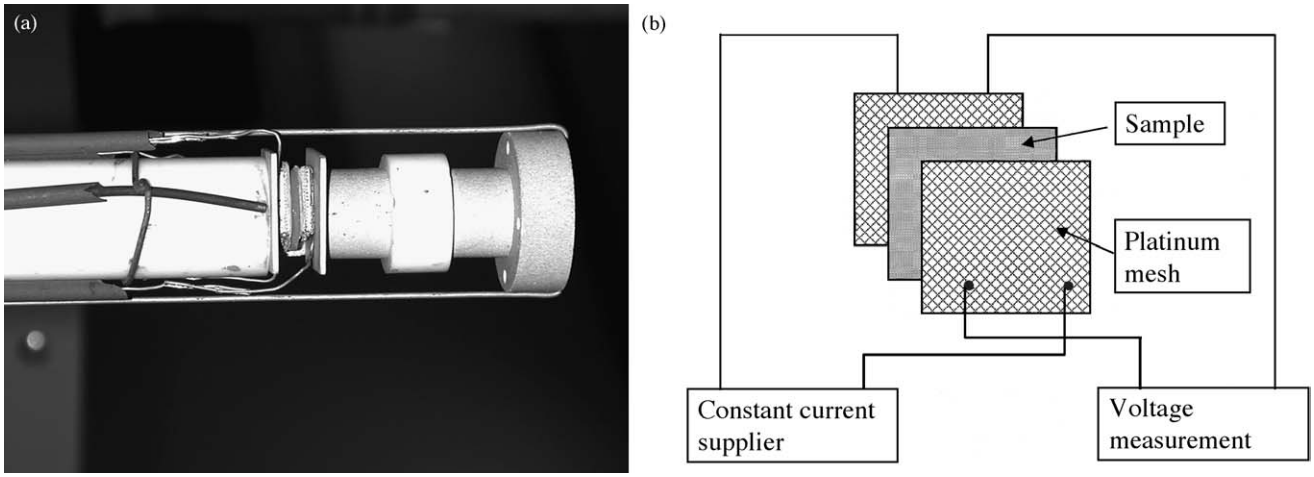

Fig. 1. (a) Resistivity measurement jig. (b) Schematic of ASR sample measurement assembly.

Table 2
Summary of XRD results for Cr_2O_3 and the spinel samples

Nominal composition	Sintering temperature (°C)	Phases detected
Cr_2O_3	1600	Cr_2O_3 (eskolaite)
$Mn_{0.5}Cr_{2.5}O_4$	1200	$MnCr_2O_4 + Cr_2O_3$
	1600	$MnCr_2O_4 + Cr_2O_3$
$MnCr_2O_4$	1200	$MnCr_2O_4$
	1600	$MnCr_2O_4 + Cr_2O_3$ (trace)
$Mn_{1.5}Cr_{1.5}O_4$	1200	$Mn_{1.5}Cr_{1.5}O_4$
	1600	$Mn_{1.5}Cr_{1.5}O_4$
Mn_2CrO_4	1200	Mn_2CrO_4
	1600	Mn_2CrO_4
$NiCr_2O_4$	1200	$NiCr_2O_4$ + NiO (trace)
	1600	$NiCr_2O_4$ + NiO (trace)
$CoCr_2O_4$	1200	$CoCr_2O_4$
	1600	$CoCr_2O_4$

Phase identification was done by indexing to files in the JCPDS database [12].

3. Results

The sintered specimens had colours ranging from yellowish green to brown to black. The colour depended on the metal oxide content; higher chromium levels led to greener tones while higher manganese levels resulted in a darker colour. Visual inspection of the specimens indicated that Mn_2CrO_4 had the largest shrinkage and a black surface.

3.1. XRD phase analysis

XRD results for the Cr_2O_3 and spinel samples are summarized in Table 2. The Cr_2O_3 sample was single phase as expected—all XRD peaks were indexed to hexagonal eskolaite. For the spinel samples, XRD patterns were virtually the same for samples sintered at 1200 and 1600 °C. In most cases, the XRD patterns were indexed as the desired cubic spinel phases only; in three instances ($Mn_{0.5}Cr_{2.5}O_4$, $MnCr_2O_4$ and $NiCr_2O_4$), however, second phases were detected. For the Cr-rich $Mn_xCr_{1-x}O_4$ samples ($Mn_{0.5}Cr_{2.5}O_4$ and $MnCr_2O_4$), the second phase was indexed as Cr_2O_3 (eskolaite). $Mn_{0.5}Cr_{2.5}O_4$ had significant amounts of Cr_2O_3, with higher amounts for the 1600 °C sample (Fig. 2a), while $MnCr_2O_4$ only had trace amounts of Cr_2O_3 and only for the 1600 °C sample. $NiCr_2O_4$ contained no Cr_2O_3, but had trace amounts of NiO (Fig. 2b).

3.2. Microstructure analysis

All spinel samples were examined using the SEM. Approximate overall Mn:Cr ratios for the Mn–Cr spinels were measured using EDX analysis (Table 3), by averaging compositions determined from at least three areas 150 μm × 150 μm in size. The Mn:Cr ratios correspond to the target compositions in all cases, except for the $Mn_{0.5}Cr_{2.5}O_4$ sample, sintered at 1600 °C. This sample had a lower Mn:Cr ratio than the target value, presumably due to the loss of Cr during sintering.

SEM micrographs from the $Mn_{0.5}Cr_{2.5}O_4$ samples, sintered at 1200 and 1600 °C, are shown in Fig. 3. Individual spinel and Cr_2O_3 phases are difficult to identify for the sample sintered at 1200 °C (Fig. 3a), but are clearly distinguishable for the sample sintered at 1600 °C. The large particles (several microns in size) in Fig. 3b contained Cr and O with virtually no Mn and are likely Cr_2O_3. The remaining, smaller particles contained Mn, Cr and O and are likely the spinel phase. The spinel particles consistently had a Cr:Mn ratio of 2:1, which suggests that the $Mn_{0.5}Cr_{2.5}O_4$ specimen was composed of $MnCr_2O_4$ and Cr_2O_3, which corroborates the XRD results.

The $MnCr_2O_4$ sample sintered at 1200 °C was composed of spinel particles only (Cr:Mn ratio of 2:1), while the 1600 °C sample was mostly spinel with isolated Cr_2O_3 particles (Fig. 4). These results match those from XRD, where only the $MnCr_2O_4$ phase was detected for the 1200 °C sample, but traces of Cr_2O_3 were found in the 1600 °C sample (Table 2).

SEM images of Mn–Cr spinel samples with higher Mn levels ($Mn_{1.5}Cr_{1.5}O_4$ and Mn_2CrO_4) are shown in Figs. 5 and 6. No Cr_2O_3 was detected, which confirms the XRD results. The microstructures are similar to the Cr-rich spinels for the lower sintering temperature (1200 °C); however, the morphology is significantly different at 1600 °C. Particle sizes are much larger for the Mn-rich spinels, exceeding 10 μm in many cases, with reduced porosity. The Mn_2CrO_4 sample, sintered at 1600 °C, was in the final stage of sintering and had almost no porosity.

SEM images for $NiCr_2O_4$ and $CoCr_2O_4$ samples are shown in Figs. 7 and 8, respectively. The microstructures are similar for both, although the $NiCr_2O_4$ samples have a larger particle size. Sintering temperature had very little effect on particle size. No additional phases (other than the spinel phases) were detected by EDX analysis, even though XRD analysis showed that the $NiCr_2O_4$ samples contained small amounts of NiO (Table 2 and Fig. 2b).

Table 3
EDX analysis of Mn:Cr ratio in spinels at various stages of preparation

Mn:Cr atomic ratio	$Mn_{0.5}Cr_{2.5}O_4$	$MnCr_2O_4$	$Mn_{1.5}Cr_{1.5}O_4$	Mn_2CrO_4
Target composition	1:5	1:2	1:1	2:1
After sintering at 1200 °C	1:5	1:2	1:1	2:1
After sintering at 1600 °C	1:3.3	1:2	1:1	2:1

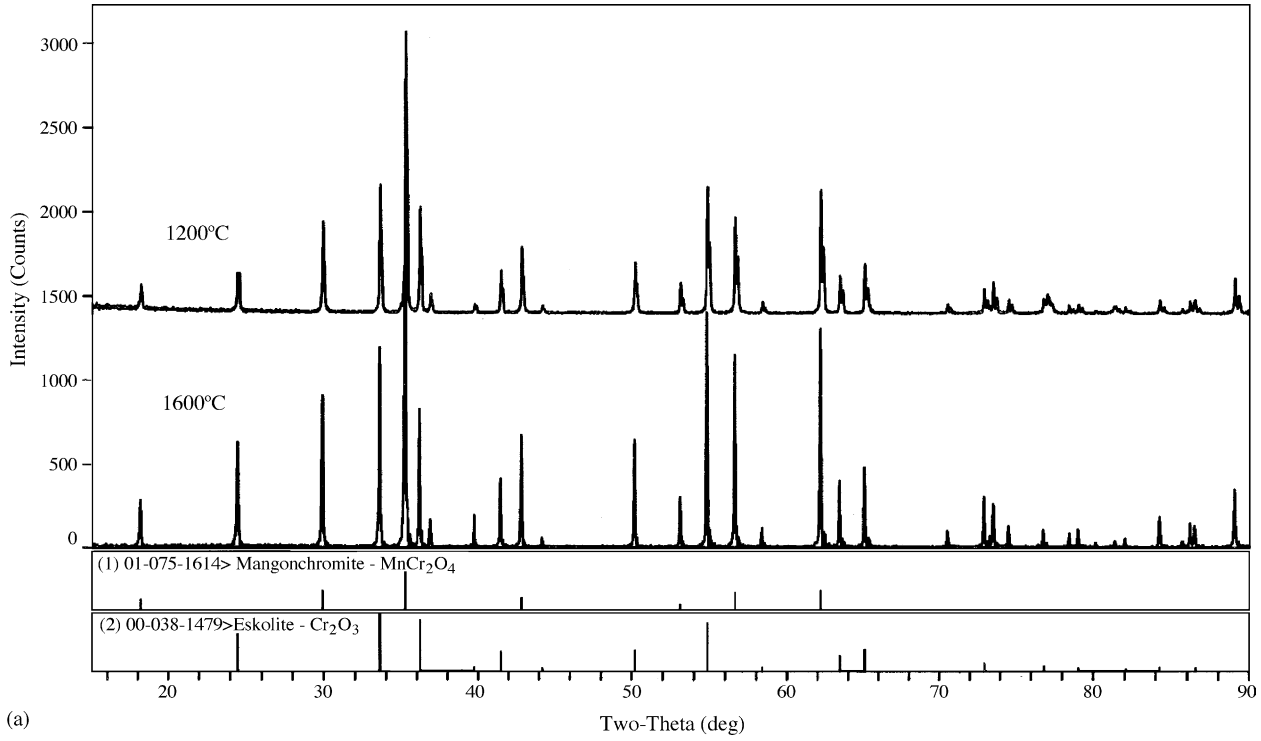

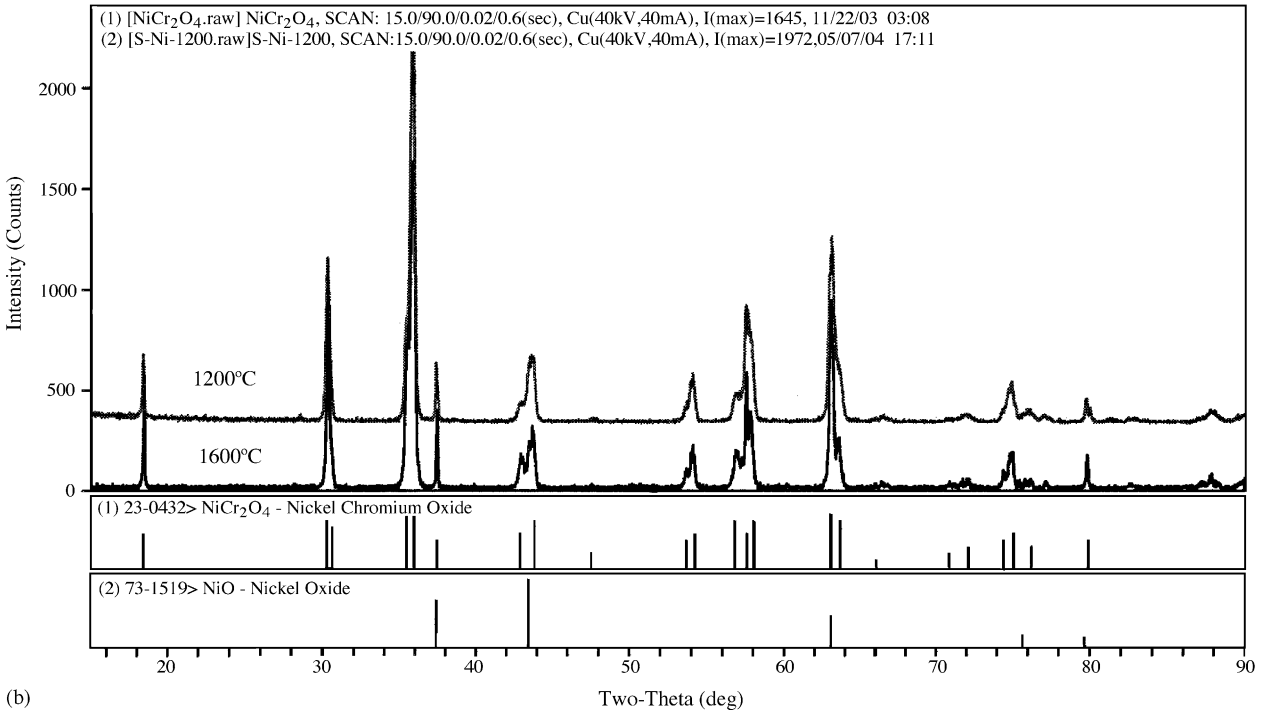

Fig. 2. XRD patterns for (a) $Mn_{0.5}Cr_{2.5}O_4$ sintered at 1200 and 1600 °C and (b) $NiCr_2O_4$ sintered 1200 and 1600 °C.

3.3. Porosity measurements

Porosity measurements, expressed as volume percents, are summarized in Table 4. The values are averaged from three measurements and have an error of ±5%. For the most part, increasing the sintering temperature leads to a reduction in porosity, with the exception of $Mn_{0.5}Cr_{2.5}O_4$ which had a lower porosity at the lower sintering temperature. Density measurements generally correlate well with SEM microstructural observations. In particular, Mn_2CrO_4 had the largest decrease in porosity, from 17 to 1%, which is also quite evident from the SEM images (Fig. 6).

Table 4
Porosities of Cr_2O_3 and spinel samples sintered at 1200 and 1600 °C

	$Mn_{0.5}Cr_{2.5}O_4$ (%)	$MnCr_2O_4$ (%)	$Mn_{1.5}Cr_{1.5}O_4$ (%)	Mn_2CrO_4 (%)	$CoCr_2O_4$ (%)	$NiCr_2O_4$ (%)	Cr_2O_3 (%)
1200 °C	17	13	16	17	20	14	
1600 °C	21	12	12	1	14	7	16

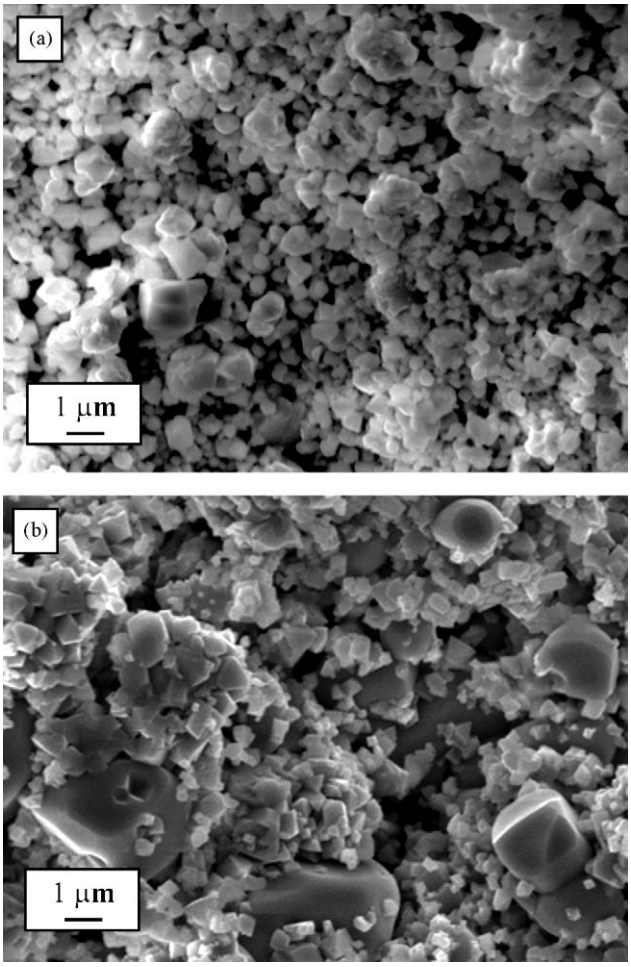

Fig. 3. SEM secondary electron (SE) images of $Mn_{0.5}Cr_{2.5}O_4$ specimens sintered at (a) 1200 °C and (b) 1600 °C.

3.4. TEC values

Thermal expansion coefficients for $MnCr_2O_4$, $CoCr_2O_4$ and $NiCr_2O_4$, sintered at 1600 °C, are shown in Table 5. The three 1600 °C sintered spinel samples had similar TEC values. For comparison, literature values for AISI-SAE 430 stainless steel (430 SS) and Cr_2O_3 are also shown in Table 5. In the temperature range of 700–900 °C, the main oxide phases forming on ferritic stainless steels surfaces are chromia (Cr_2O_3) and spinels. A good TEC match between components would reduce thermal stresses, which might otherwise cause structurally layered materials to delaminate or spall locally. Chromia has a better TEC match with the stainless steel, relative to any of the spinel phases.

Table 5
TEC values for the spinel samples, chromia and 430 SS

TEC	$\alpha \times 10^{-6}$ (°C^{-1})
430 SS	11.4 [13] (25–500 °C)
$MnCr_2O_4$	7.2 (25–900 °C)
$CoCr_2O_4$	7.4 (25–900 °C)
$NiCr_2O_4$	7.6 (25–900 °C)
Cr_2O_3	9.6 [14] (25–1400 °C)

All samples were sintered at 1600 °C.

3.5. Resistivity measurements

Figs. 9 and 10 show plots of resistivity versus $1/T$ for Cr_2O_3 and the various spinel samples, sintered at 1600 °C. The error range for Cr_2O_3 values is ±9%; error ranges for all other measurements are less than ±5 %. The data shown in Figs. 9 and 10 are corrected for porosity, by dividing measured resisitivities by the corresponding bulk density fractions (~80–100%). This approach was based on the assumption that resistivities vary linearly with porosity for the porosities exhibited in this work. The resistivities show linear behaviour with $1/T$, over a wide range of temperatures, which is indicative of semiconductor behaviour. All samples, except for chromia, $CoCr_2O_4$ and Mn_2CrO_4, show a slope change at an intermediate temperature. The cause of the slope change is not clear at this time, but may be associated with a phase change.

Table 6 shows a summary of resistivities (corrected for porosity) measured at 750 °C for the various spinel samples and Cr_2O_3, after sintering at 1200 and 1600 °C. The table also includes selected data from the literature. According to a summary by Kofstad [15], resistivity values for Cr_2O_3 in

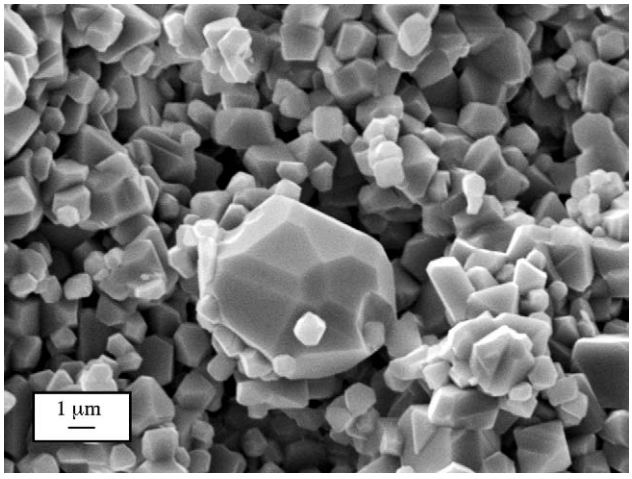

Fig. 4. SEM SE image of $MnCr_2O_4$ specimen sintered at 1600 °C. The larger particle is Cr_2O_3.

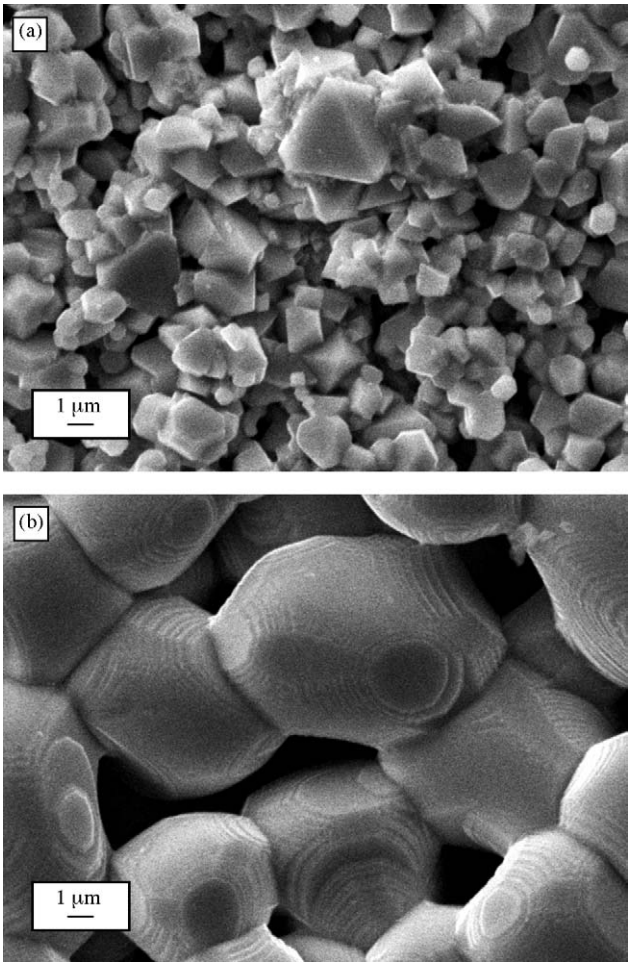

Fig. 5. SEM back scattered electron (BSE) images of $Mn_{1.5}Cr_{1.5}O_4$ specimens sintered at (a) 1200 °C and (b) 1600 °C.

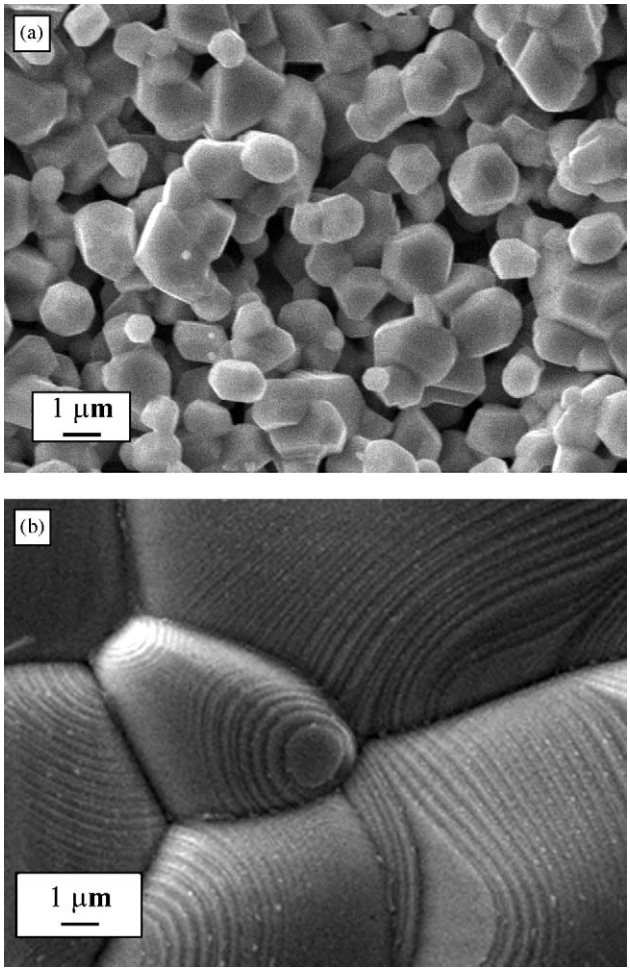

Fig. 6. SEM BSE images of Mn_2CrO_4 specimens sintered at (a) 1200 °C and (b) 1600 °C.

the literature are generally reported to be in the 0.1–1.0 Ωm range (in agreement with the value reported here), with the exception of the value of 180 Ωm reported by Virkar and England [16].

Widely spread resistivities for $MnCr_2O_4$ are reported in the literature. The data from England [17] showed a similar trend to the results in this work. The resistivities for $MnCr_2O_4$ and Mn_2CrO_4, measured at 800 °C, were 19.5 and 0.035 Ωm, respectively. Both of their spinel samples were sintered in nitrogen and resistivities were measured with a two-point probe. A very low resistivity for $MnCr_2O_4$ of 0.072 Ωm was reported by Virkar and England [16] in their patent. However, there seems to be some confusion in the patent about which Mn–Cr spinel was tested, with the authors referring to the spinel as $Mn_{1.5}Cr_{1.5}O_4$ in the text and $MnCr_2O_4$ in their resistivity plot. It may be that resistivities were measured for $Mn_{1.5}Cr_{1.5}O_4$ and not $MnCr_2O_4$, putting their values more in line with the ones presented here.

4. Discussion

4.1. Mn–Cr spinel samples

4.1.1. Phase analysis

The Mn_2O_3–Cr_2O_3 phase diagram is shown in Fig. 11 [10], along with the compositions of the Mn–Cr oxide

Table 6
Comparison of literature and measured resistivity (Ωm) values for spinel samples and chromia at 750 °C

	$Mn_{0.5}Cr_{2.5}O_4$	$MnCr_2O_4$	$Mn_{1.5}Cr_{1.5}O_4$	Mn_2CrO_4	$CoCr_2O_4$	$NiCr_2O_4$	Cr_2O_3
Sintered at 1200 °C	2.16	3.23	0.62	0.078	0.53	0.016	
Sintered at 1600 °C	6.59	7.86	0.23	0.033	0.51	0.016	0.20
Virkar and England [16]		0.072					180
England [17]		19.5 (800 °C)		0.035 (800 °C)			
The Oxide Handbook [14]							0.78

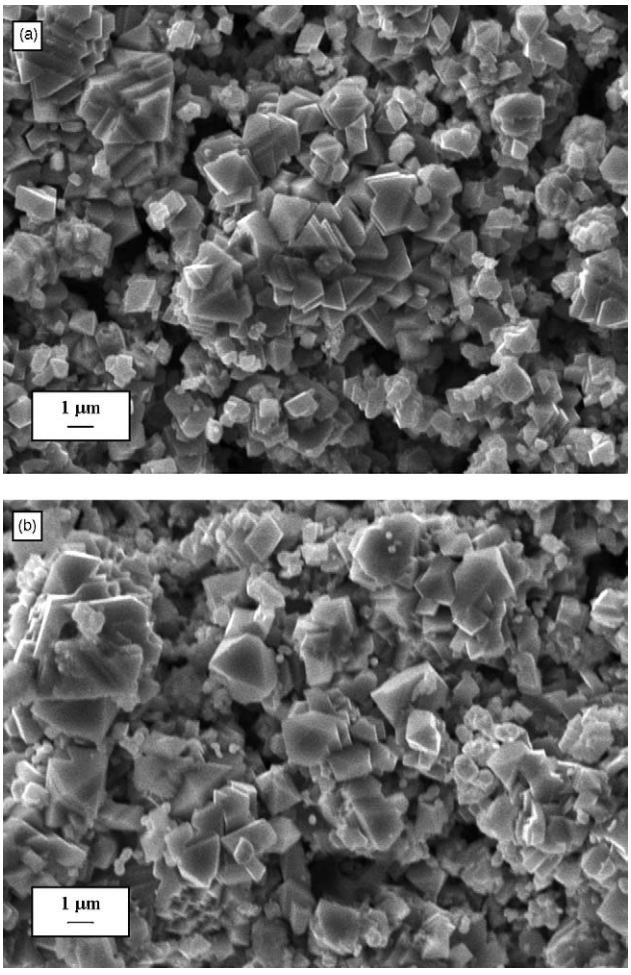

Fig. 7. SEM SE images of $NiCr_2O_4$ specimens sintered at (a) 1200 °C and (b) 1600 °C.

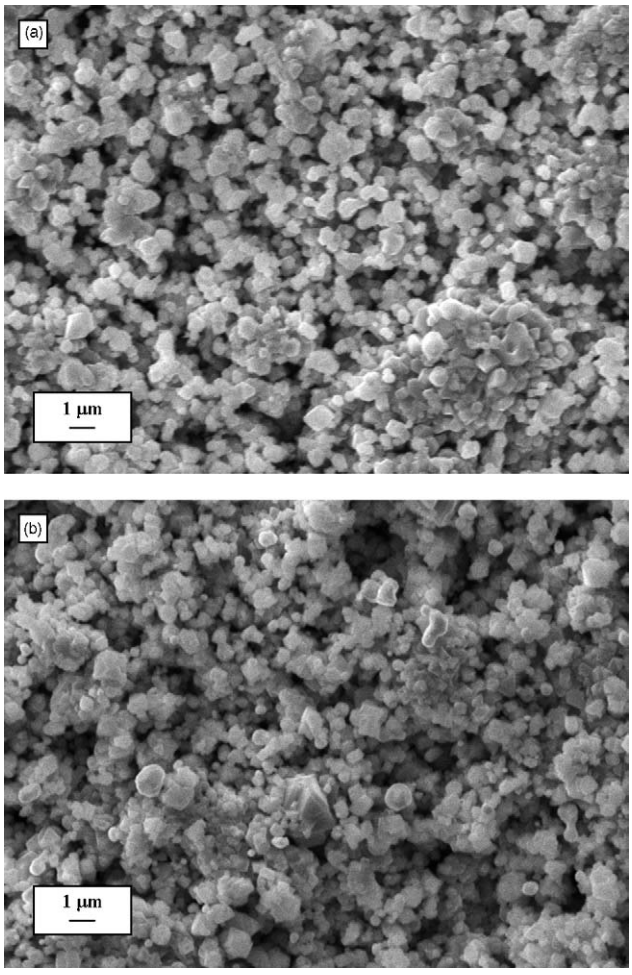

Fig. 8. SEM SE images of $CoCr_2O_4$ specimens sintered at (a) 1200 °C and (b) 1600 °C.

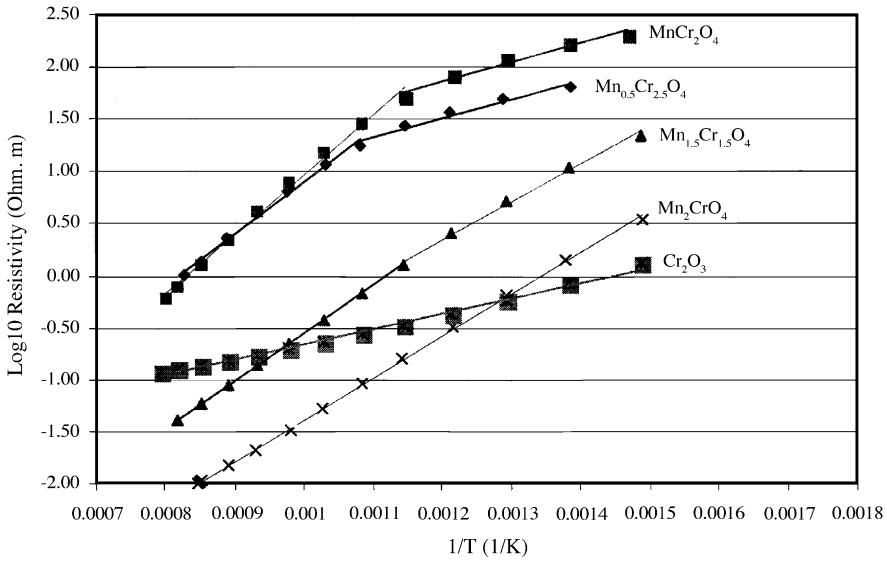

Fig. 9. Resistivity as a function of temperature for chromia and $Mn_xCr_{(3-x)}O_4$ spinel samples, sintered at 1600 °C.

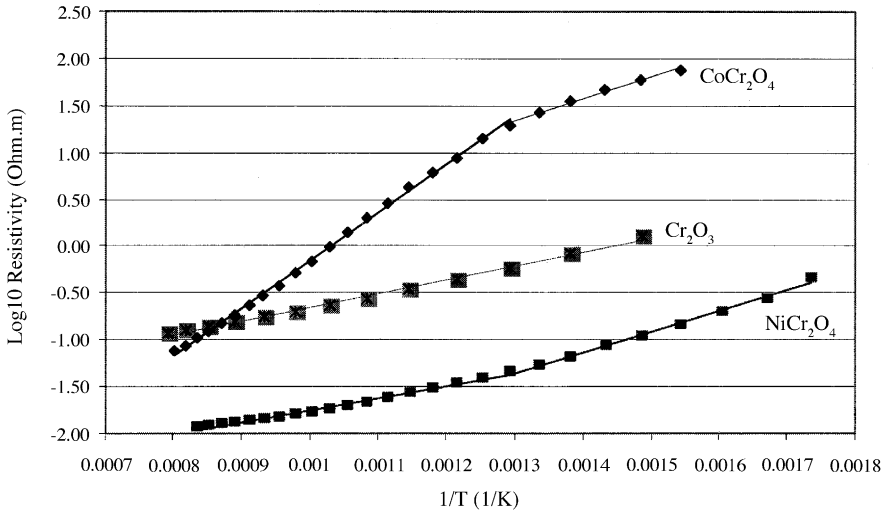

Fig. 10. Resistivity as a function of temperature for chromia, $NiCr_2O_4$ and $CoCr_2O_4$, sintered at 1600 °C.

specimens prepared; these are indicated by positions 1, 2, 3 and 4. These numbers correspond to Mn_2CrO_4, $Mn_{1.5}Cr_{1.5}O_4$, $MnCr_2O_4$ and $Mn_{0.5}Cr_{2.5}O_4$ spinel compositions, respectively. Note that the single phase, spinel region is stable over a wide composition range (~0–60 wt.% Cr_2O_3) at selected temperatures.

Samples with compositions corresponding to positions 1 and 2, i.e., Mn_2CrO_4 and $Mn_{1.5}Cr_{1.5}O_4$, should, based on this diagram, produce a single spinel phase at either sintering temperature, 1200 or 1600 °C. The spinel phase is not thermodynamically stable at room temperature; eutectoid decomposition to Mn_2O_3 and Cr_2O_3 is expected at ~525–530 °C. However, because of kinetic limitations, decomposition of the spinel phase is unlikely for the experimental conditions used here. This assumption is borne out here for Mn_2CrO_4 and $Mn_{1.5}Cr_{1.5}O_4$, as both the XRD and SEM results show

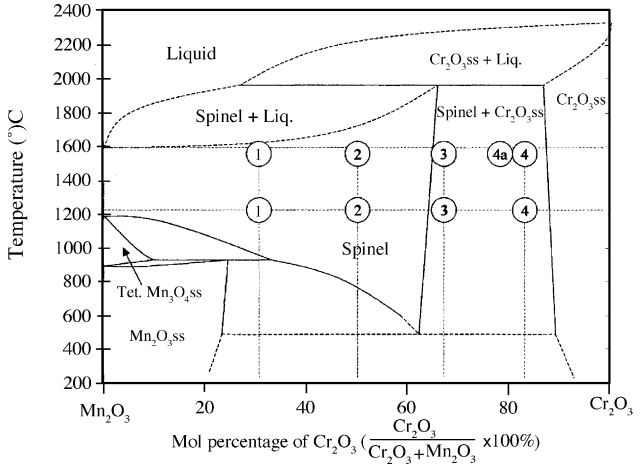

Fig. 11. Phase diagram for Mn_2O_3–Cr_2O_3 system (ss: solid solution; Tet.: tetragonal; Liq.: liquid). The numbers 1, 2, 3 and 4 refer to the nominal compositions of the prepared spinel samples, i.e., Mn_2CrO_4, $Mn_{1.5}Cr_{1.5}O_4$, $MnCr_2O_4$ and $Mn_{0.5}Cr_{2.5}O_4$, respectively. Modified phase diagram from The American Ceramic Society, www.ceramics.org.

that only a single spinel phase is present. For both Mn_2CrO_4 and $Mn_{1.5}Cr_{1.5}O_4$, the chemical formulas are more accurately depicted as $Mn(MnCr)O_4$ and $Mn(Mn_{0.5}Cr_{1.5})O_4$. The Mn in the brackets has a valence of 3+, while the Mn outside the brackets has a valence of 2+. Partial substitution of Mn^{3+} for Cr^{3+} leads to a slight increase in the cubic lattice parameter (and therefore the interplanar spacings), since the ionic radius for Mn^{3+} (0.066 nm) is slightly larger than that for Cr^{3+} (0.063 nm).

For the composition corresponding to $Mn_{0.5}Cr_{2.5}O_4$ or position 4 on the phase diagram, the sample should be primarily chromia with some spinel (~20%), assuming no decomposition of the spinel phase to Mn_2O_3 and Cr_2O_3 below the eutectoid temperature. From the XRD results (Fig. 2a), both chromia and spinel were present in significant quantities, but the amount of spinel was in excess of 20%. The reason for this discrepancy may be related to the composition information obtained through EDX analysis in the SEM (Table 3). For the sample sintered at 1600 °C, actual Cr levels were lower than the nominal $Mn_{0.5}Cr_{2.5}O_4$ composition, putting the composition at position 4a on the phase diagram. Based on position 4a, the relative amounts of chromia and spinel should be comparable, which agrees well with the XRD results (Fig. 2a and Table 3). The apparent loss of Cr on sintering may be due to the evaporation of chromia at elevated temperatures as reported in the literature [18].

$$2Cr_2O_3\,(s) + 3O_2\,(g) \Leftrightarrow 4CrO_3\,(g) \quad (2)$$

The loss of Cr would drive the overall sample composition to the left (Mn-rich) side of the phase diagram (from position 4 to position 4a in Fig. 11) resulting in more spinel phase as observed in this work. In addition, the loss of Cr should be more prevalent at 1600 °C due to the higher CrO_3 vapor pressure.

For $MnCr_2O_4$ or composition 3 on the phase diagram, the sample should consist of two phases, i.e., mostly spinel with a small amount of chromia. This agrees well with the XRD

results in Table 2 and SEM results in Fig. 4, where only a trace amount of chromia was detected—the majority phase was spinel.

4.1.2. Porosity and crystal morphology

SEM results from samples sintered at 1600 °C showed well-developed crystal facets and qualitatively less porosity relative to samples sintered at 1200 °C (Figs. 3–6). Samples sintered at 1200 °C showed signs of interdiffusion between the particles, as evidenced by neck formation, but the particle size is generally smaller, and necking less developed, relative to the higher sintering temperature.

There was a general decrease in porosity for higher sintering temperatures, with the effect becoming more pronounced at higher Mn levels (Table 4). The exception was the $Mn_{0.5}Cr_{2.5}O_4$ sample, where the porosity was higher for sintering at 1600 °C. The previous discussion indicates that the $Mn_{0.5}Cr_{2.5}O_4$ sample consists of two phases, spinel plus a significant amount of Cr_2O_3. Chromia can evaporate, particularly at the higher sintering temperature, which could account for the increased porosity. For the $MnCr_2O_4$ sample (Table 4), the porosities are almost the same for the two sintering temperatures. The expected decrease in porosity due to better sintering at 1600 °C may be offset by some evaporation of the limited amount of chromia present.

4.1.3. Resistivities

Resistivities at 750 °C (corrected for porosity) for the Mn–Cr spinels are plotted as a function of oxide composition (the same format as used for the phase diagram) in Fig. 12. The resistivities for both the 1200 and 1600 °C sintered samples increase with increasing Cr content until composition 3, whereupon the resistivities decrease slightly thereafter. Compositions 1 and 2 correspond to Mn_2CrO_4 and $Mn_{1.5}Cr_{1.5}O_4$, respectively, and represent single-phase spinel regions. It is clear that increasing the Cr level in the spinel phase increases its resistivity. For compositions 1 and 2, the effect of sintering temperature is likely related to particle or grain size; the higher sintering temperature (1600 °C) produces a coarser microstructure (Figs. 5 and 6) with fewer grain boundaries (fewer charge carrier scattering centres), and therefore lower resistivities. Composition 3 corresponds to the appearance of chromia in the samples. Here, the resistivity levels out and then decreases with increasing Cr levels for both sintering temperatures. This corresponds to increasing amounts of chromia, which has a lower resistivity than high Cr-containing spinels (Fig. 9; Table 6). The effect of sintering temperature for compositions 3 and 4 is opposite to that observed for compositions 1 and 2. The resistivities are higher for both samples sintered at 1600 °C. The sample corresponding to composition 4 (or 4a for the actual composition) should have less chromia for a sintering temperature of 1600 °C, relative to 1200 °C, due to increased Cr evaporation, which could account for the higher resistivity.

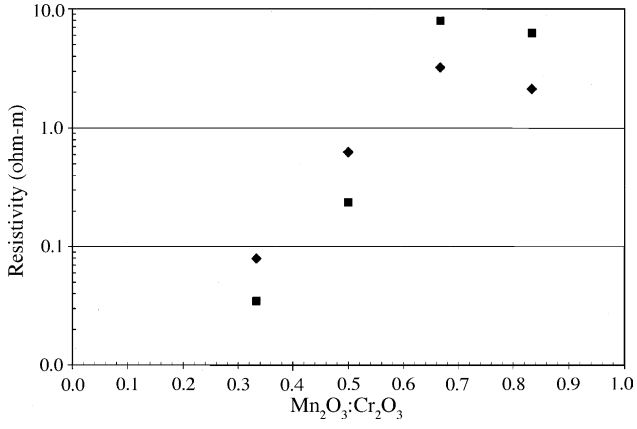

Fig. 12. Plot of resistivity at 750 °C vs. Mn_2O_3–Cr_2O_3 composition for samples sintered at 1200 °C (♦) and 1600 °C (■).

4.2. $NiCr_2O_4$ and $CoCr_2O_4$

NiO–Cr_2O_3 and CoO–Cr_2O_3 phase diagrams were not available in the published literature, so direct phase analysis as was done with the Mn–Cr spinels was not possible. $CoCr_2O_4$ was single phase, as confirmed by XRD analysis, with very little difference in morphology (other than particle size) for the two sintering temperatures. $NiCr_2O_4$ was primarily single phase, with only trace amounts of NiO. Whether NiO arises from sample preparation or from phase separation during sintering is not clear from this study.

Resistivity results in Table 6 showed, after porosity compensation, similar values for both 1200 and 1600 °C. $NiCr_2O_4$ samples had the lowest resistivities compared with all other samples including Cr_2O_3. The resistivity at 750 °C was 0.016 Ωm, which is more than order of magnitude better than the lowest values for the best Mn–Cr spinels. $CoCr_2O_4$, on the other hand, had resistivity values consistently higher than Cr_2O_3, except at the highest test temperatures, with values similar to the best Mn–Cr spinels (Fig. 10).

5. Summary

Several spinel samples, i.e., $Mn_xCr_{3-x}O_4$ ($0.5 \leq x \leq 2.5$), $NiCr_2O_4$ and $CoCr_2O_4$, were synthesized and studied in terms of phase analysis, density, resistivity and thermal expansion behaviour. The following results were obtained:

- The spinel samples were generally single phase. The exceptions were $MnCr_2O_4$ and $Mn_{0.5}Cr_{2.5}O_4$ with significant amounts of Cr_2O_3 and $NiCr_2O_4$ with trace amounts of NiO.
- Porosity, in general, decreased with increasing sintering temperature. The exception was $Mn_{0.5}Cr_{2.5}O_4$, which had more porosity for the higher sintering temperature. This was attributed to evaporation of Cr_2O_3.
- $NiCr_2O_4$, $CoCr_2O_4$ and $MnCr_2O_4$ all had similar thermal expansion behaviour, with TEC values equal to

7.2–7.6 $\times 10^{-6}$/°C. The TEC difference between the spinels and ferritic stainless steel (430 SS) was larger than the difference between the steel and chromia, which has a TEC of 9.6 $\times 10^{-6}$/°C.

- The spinels and chromia exhibited semiconductor-type behaviour, with electrical resistivities decreasing with increasing temperature. Only Mn_2CrO_4 and $NiCr_2O_4$ had resistivities lower than Cr_2O_3 over the entire temperature range of testing (20–900 °C). $NiCr_2O_4$ had the lowest resistivities.
- For $Mn_xCr_{2-x}O_4$, resistivity decreased with increasing Mn content.

Acknowledgements

The authors are grateful to the Natural Sciences and Engineering Research Council (NSERC) of Canada, the Alberta Energy Research Institute (AERI) Core University Research in Sustainable Energy (COURSE) program and Versa Power Systems (VPS). VPS is also acknowledged for supplying materials and providing access to processing and testing facilities. The authors would like to thank E. Tang, A. Wood and J. Protkova of VPS for their technical and experimental assistance.

References

[1] W.J. Quadakkers, J. Piron-Abellan, V. Shemet, L. Singheiser, Metallic interconnectors for solid oxide fuel cells—a review, Mater. High Temp. 20 (2) (2003) 115–127.
[2] T. Horita, Y. Xiong, H. Kishimoto, K. Yamaji, N. Sakai, H. Yokokawa, Application of Fe–Cr alloys to solid oxide fuel cells for cost-reduction: oxidation behaviour of alloys in methane fuel, J. Power Sources 131 (1–2) (2004) 293–298.
[3] H. Kurokawa, K. Kawamura, T. Maruyama, Oxidation behavior of Fe-16cr alloy interconnect for SOFC under hydrogen potential gradient, Solid State Ionics 168 (1–2) (2004) 13–21.
[4] T. Horita, Y. Xiong, K. Yamaji, N. Sakai, H. Yokokawa, Stability of Fe–Cr Alloy interconnects under CH_4–H_2O atmosphere for SOFCs, J. Power Sources 118 (1–2) (2003) 35–43.
[5] W.Z. Zhu, S.C. Deevi, Development of interconnect materials for solid oxide fuel cells, Mater. Sci. Eng. A 348 (1–2) (2003) 227–243.
[6] T.J. Armstrong, Micheal A. Homel, Anil V. Virkar, Evaluation of Metallic Interconnects for Use in Intermediate Temperature SOFC, Solid Oxide Fuel Cells VIII, vol. PV 2003-07, The Electrochemical Society, Pennington, NJ, 2003, pp. 841–850.
[7] K. Huang, P.Y. Hou, J.B. Goodenough, Reduced area specific resistance for iron based metallic interconnects by surface oxide coatings. Mater. Res. Bull. 36 (1–2) (2001) 81–95.
[8] S.C. Kung, Performance of metallic interconnect in solid oxide fuel cells, Portland, Oregon, 30 October–2 November 2000, pp. 585–588.
[9] The Spinel Group of Minerals, Amethyst Galleries Inc., http://mineral.galleries.com/minerals/oxides/spinel.htm, July 2004.
[10] Phase Equilibria Diagrams Database, National Institute of Standards and Technology, American Ceramic Society, Version 2.1 for Windows 95.
[11] E.N. Kaufmann, Characterization of Materials, vol. 1, John Wiley & Sons Ltd., New Jersey, 2003, p. 1392.
[12] JADE Version 7 Software—XRD Processing, Identification and Quantification, Materials Data Inc., 2004.
[13] J.R. Davis (Ed.), Metals Handbook, Desk Ed., ASM International, Ohio, 1998, p. 1521.
[14] G.V. Samsonov (Ed.), The Oxide Handbook, Plenum Data Corporation, New York, 1973, p. 524.
[15] P. Kofstad, Nonstoichiometry, Diffusion, and Electrical Conductivity in Binary Metal Oxides, Robert E. Krieger Publishing Company, Florida, 1983.
[16] A.V. Virkar, D.M. England, US 6,054,231, Solid Oxide Fuel Cell Interconnector.
[17] D.M. England, A metallic interconnect for a solid oxide fuel cell stack, in Department of Materials Science and Engineering, Ph. D. thesis, The University of Utah, 2003.
[18] A. Yamauchi, K. Kurokawa, H. Takahashi, Evaporation of Cr_2O_3 in atmospheres containing H_2O, Oxidation Metals 59 (5–6) (2003) 517–527.